

# THE FREQUENCY OF INTRINSIC X-RAY WEAKNESS AMONG BROAD ABSORPTION LINE QUASARS

HEZHEN LIU<sup>1,2,3</sup>, B. LUO<sup>1,2,3</sup>, W. N. BRANDT<sup>4,5,6</sup>, S. C. GALLAGHER<sup>7</sup>, G. P. GARMIRE<sup>8</sup>

*Draft version April 17, 2018*

## ABSTRACT

We present combined  $\approx 14\text{--}37$  ks *Chandra* observations of seven  $z = 1.6\text{--}2.7$  broad absorption line (BAL) quasars selected from the Large Bright Quasar Survey (LBQS). These seven objects are high-ionization BAL (HiBAL) quasars, and they were undetected in the *Chandra* hard band (2–8 keV) in previous observations. The stacking analyses of previous *Chandra* observations suggested that these seven objects likely contain some candidates for intrinsically X-ray weak BAL quasars. With the new *Chandra* observations, six targets are detected. We calculate their effective power-law photon indices and hard-band flux weakness, and find that two objects, LBQS 1203+1530 and LBQS 1442–0011, show soft/steep spectral shapes ( $\Gamma_{\text{eff}} = 2.2^{+0.9}_{-0.9}$  and  $1.9^{+0.9}_{-0.8}$ ) and significant X-ray weakness in the hard band (by factors of  $\approx 15$  and 12). We conclude that the two HiBAL quasars are good candidates for intrinsically X-ray weak BAL quasars. The mid-infrared-to-UV spectral energy distributions (SEDs) of the two candidates are consistent with those of typical quasars. We constrain the fraction of intrinsically X-ray weak AGNs among HiBAL quasars to be  $\approx 7\text{--}10\%$  (2/29–3/29), and we estimate it is  $\approx 6\text{--}23\%$  (2/35–8/35) among the general BAL quasar population. Such a fraction is considerably larger than the fraction among non-BAL quasars, and we suggest that intrinsically X-ray weak quasars are preferentially observed as BAL quasars. Intrinsically X-ray weak AGNs likely comprise a small minority of the luminous type 1 AGN population, and they should not affect significantly the completeness of these AGNs found in deep X-ray surveys.

**Keywords:** galaxies: active – quasars: absorption lines – X-rays: general

## 1. INTRODUCTION

X-ray emission is a characteristic property of active galactic nuclei (AGNs), and it is generally believed to be produced within an accretion-disk corona by inverse-Compton scattering of accretion-disk optical/UV photons (e.g., Done 2010; Gilfanov & Merloni 2014; Fabian et al. 2017). Previous studies have shown that the UV and X-ray luminosities of AGNs are related, and this relation is quantified as the anti-correlation between the 2500 Å monochromatic luminosity ( $L_{2500\text{ Å}}$ ) and X-ray-to-optical power-law slope ( $\alpha_{\text{OX}}$ )<sup>9</sup> across  $\approx 5$  orders of magnitude in UV luminosity (e.g., Steffen et al. 2006; Just et al. 2007; Lusso et al. 2010). This observed relation indicates some underlying physical mechanisms working to balance the emission of accretion disks and coronae. Since the observed X-ray emission could have contributions from AGN jets (e.g., Miller et al. 2011), and it could also be modified by photoelectric absorption, studies

of the  $\alpha_{\text{OX}}\text{--}L_{2500\text{ Å}}$  relation usually exclude radio-loud AGNs and potentially X-ray absorbed AGNs, e.g., broad absorption line (BAL) quasars.

Few AGNs are found to be intrinsically X-ray weak, emitting much less X-ray radiation than expected from the  $\alpha_{\text{OX}}\text{--}L_{2500\text{ Å}}$  relation. For example, Gibson et al. (2008) systematically investigated the X-ray and UV properties of optically selected, radio-quiet, and non-BAL type 1 quasars. Their results showed that the fraction of luminous AGNs that are intrinsically X-ray weak by a factor of  $\approx 10$  is  $\lesssim 2\%$ . Therefore, it has been challenging to identify intrinsically X-ray weak AGNs. One well-studied example is PHL 1811, which is a bright nearby ( $z = 0.192$ ) type 1 quasar with a *B*-band magnitude of 13.9. Its observed X-ray emission is weaker than the expectation from the  $\alpha_{\text{OX}}\text{--}L_{2500\text{ Å}}$  relation by a factor of  $\approx 30\text{--}100$ , and its soft X-ray spectrum (with a power-law photon index  $\Gamma \approx 2.3$ ) and short-term X-ray variability argue against an absorption scenario (e.g., Leighly et al. 2007a,b). Thus it is believed to be intrinsically X-ray weak. Recently, X-ray studies of less-massive black-hole (BH) systems ( $M_{\text{BH}} \approx 10^4\text{--}10^6 M_{\odot}$ ) have suggested a few candidates for intrinsically X-ray weak AGNs (e.g., Plotkin et al. 2016; Simmonds et al. 2016).

The identification of intrinsically X-ray weak AGNs has considerable importance. It challenges the ubiquity of luminous X-ray emission from AGNs, which is central to the utility of X-ray surveys for finding AGNs throughout the Universe (e.g., Brandt & Alexander 2015). Studies of intrinsically X-ray weak AGNs might also provide insights into the physics of the X-ray corona. To obtain the frequency of these rare and extreme AGNs and understand better their nature, it is critical to identify more intrinsically X-ray weak AGNs and to characterize their X-ray and multiwavelength properties.

There are two criteria for identifying an intrinsically X-ray weak AGN: it must be X-ray weak (relative to the

<sup>1</sup> School of Astronomy and Space Science, Nanjing University, Nanjing, Jiangsu 210093, China

<sup>2</sup> Key Laboratory of Modern Astronomy and Astrophysics (Nanjing University), Ministry of Education, Nanjing 210093, China

<sup>3</sup> Collaborative Innovation Center of Modern Astronomy and Space Exploration, Nanjing 210093, China

<sup>4</sup> Department of Astronomy and Astrophysics, 525 Davey Lab, The Pennsylvania State University, University Park, PA 16802, USA

<sup>5</sup> Institute for Gravitation and the Cosmos, The Pennsylvania State University, University Park, PA 16802, USA

<sup>6</sup> Department of Physics, 104 Davey Lab, The Pennsylvania State University, University Park, PA 16802, USA

<sup>7</sup> Department of Physics & Astronomy and Centre for Planetary and Space Exploration, The University of Western Ontario, London, ON, N6A 3K7, Canada

<sup>8</sup> Huntingdon Institute for X-ray Astronomy, LLC

<sup>9</sup>  $\alpha_{\text{OX}}$  is used to compare the optical/UV and X-ray luminosities and it is defined as  $\alpha_{\text{OX}} = 0.3838 \log(f_{2\text{keV}}/f_{2500\text{ Å}})$ , where  $f_{2\text{keV}}$  and  $f_{2500\text{ Å}}$  are the flux densities at rest-frame 2 keV and 2500 Å.

$\alpha_{\text{OX}}-L_{2500 \text{ \AA}}$  relation) and its X-ray weakness must be not entirely accounted for by absorption. BAL quasars are generally observed to be X-ray weak, with the X-ray weakness often attributed to absorption due to their often hard X-ray spectral shapes (e.g., Gallagher et al. 2002, 2006; Fan et al. 2009; Gibson et al. 2009). In the accretion-disk wind models for BAL quasars (e.g., Murray et al. 1995; Proga et al. 2000), the BALs are produced in an outflowing wind that is driven by UV radiation pressure. In the commonly considered smooth wind scenario (Murray et al. 1995), some shielding material is required to protect the wind from overionization by the nuclear ionizing radiation, so that the wind can be driven out effectively by radiation pressure. The observed X-ray emission could thus be absorbed by the shielding gas. In a clumpy wind scenario (e.g., Baskin et al. 2014; Matthews et al. 2016), the wind can be launched successfully without the requirement of shielding gas. However, the clumpy outflows themselves could cause X-ray absorption. Therefore, BAL quasars are often considered to be X-ray absorbed, and they have usually been excluded in previous searches for intrinsically X-ray weak AGNs.

On the other hand, if somehow a BAL quasar is intrinsically X-ray weak, the outflowing wind, whether smooth or clumpy, can be launched without fear of overionization, leading to the observed BALs and X-ray weakness. Indeed, through *NuSTAR* hard X-ray (3–24 keV) observations of several significantly X-ray weak BAL quasars, a few candidates for intrinsically X-ray weak BAL quasars have been suggested (Luo et al. 2013, 2014; Teng et al. 2014); most of these objects have soft effective power-law photon indices ( $\Gamma_{\text{eff}} \approx 1.8$ ) in the 3–24 keV band on average (via stacking analysis), disfavoring the absorption scenario.

Motivated by the *NuSTAR* results, Luo et al. (2013) re-investigated the X-ray properties of a well-defined *Chandra* sample of 35 high-redshift ( $z \approx 1.5$ –3) BAL quasars in Gallagher et al. (2006), which were selected from the Large Bright Quasar Survey (LBQS) sample (e.g., Hewett et al. 1995; Hewett & Foltz 2003). At the mean redshift of  $z \approx 2$  for these BAL quasars, the 0.5–8 keV *Chandra* observations sample rest-frame  $\approx 1.5$ –24 keV X-rays, close to the hard X-ray band observed by *NuSTAR* for low-redshift targets. Stacking analyses of the 12 hard-band (2–8 keV) undetected objects also revealed a soft effective photon index in the rest-frame  $\approx 1.5$ –24 keV band ( $\Gamma_{\text{eff}} \approx 1.6$ ; e.g., Figure 9 of Luo et al. 2013), suggestive of the presence of intrinsically X-ray weak BAL quasars among this high-redshift sample. Based on these results, a fraction of  $\approx 17$ –40% for intrinsically X-ray weak AGNs among BAL quasars was estimated, which is apparently much higher than that of intrinsically X-ray weak AGNs among non-BAL quasars (Gibson et al. 2008).

The presence of intrinsically X-ray weak BAL quasars among the LBQS sample was suggested by the Luo et al. (2013) stacking analyses. We could not identify such objects individually, and their fraction among BAL quasars was poorly constrained. In this paper, we analyze additional *Chandra* observations of seven of the 12 hard-band undetected BAL quasars, including six new *Chandra* Cycle 16 observations and one new *Chandra* archival observation. We introduce *Chandra* identification of intrinsic X-ray weakness and sample selection in Section 2. The X-ray data analyses are described in Section 3. We present the results and the two good candidates for intrinsically X-ray weak BAL quasars in Section 4. We discuss implications in Section 5, and we summarize in Section 6. Through-

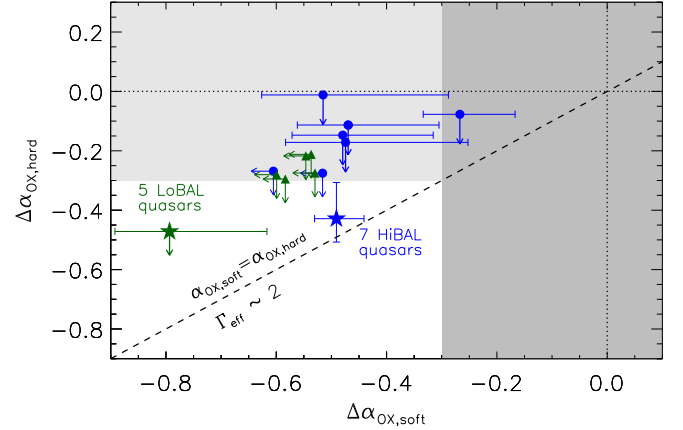


**Figure 1.**  $\Delta\alpha_{\text{OX,hard}}$  versus  $\Delta\alpha_{\text{OX,soft}}$  for the 12 hard-band undetected LBQS BAL quasars in Gallagher et al. (2006), including seven HiBAL and five LoBAL quasars, shown as blue dots and green triangles, respectively. Upper limits on  $\Delta\alpha_{\text{OX,soft}}$  ( $\Delta\alpha_{\text{OX,hard}}$ ) are shown as arrows when objects are undetected in the soft (hard) X-ray band. The stacked source of the HiBAL (LoBAL) quasars is shown as the blue star (green star). The dark and light shaded regions show the  $\approx 95\%$  ( $\approx 2\sigma$ ) confidence-level uncertainties of  $\alpha_{\text{OX,exp}}$ . The slanted dashed line indicates  $\alpha_{\text{OX,soft}} = \alpha_{\text{OX,hard}}$  and  $\Gamma_{\text{eff}} \approx 2$ . Objects lying outside the shaded regions are significantly X-ray weak, and objects lying near the slanted line have soft spectra.

out this paper, we use J2000 coordinates and a cosmology with  $H_0 = 67.8 \text{ km s}^{-1} \text{ Mpc}^{-1}$ ,  $\Omega_M = 0.308$ , and  $\Omega_\Lambda = 0.692$  (Planck Collaboration et al. 2016).

## 2. IDENTIFICATION OF INTRINSICALLY X-RAY WEAK AGNS AND SAMPLE SELECTION

It has been challenging to identify intrinsically X-ray weak AGNs, mainly because it is difficult to determine if the observed X-ray weakness results from absorption or intrinsic X-ray weakness. Spectral fitting of a  $\lesssim 8$  keV X-ray spectrum may not be sufficient to recover the intrinsic X-ray emission if there is complex absorption present. For example, if an AGN is obscured by a Compton-thick absorber ( $N_H \geq 1.5 \times 10^{24} \text{ cm}^{-2}$ ), and its  $\lesssim 8$  keV X-ray spectrum is dominated by a possible scattered/reflected soft component, spectral fitting of the  $\lesssim 8$  keV X-ray spectrum may not necessarily reveal the Compton-thick absorption (see, e.g., Comastri 2004 for a review). Therefore, a soft  $\lesssim 8$  keV spectrum does not necessarily rule out absorption. Indeed, the intrinsic X-ray weakness of PHL 1811 (see Section 1) is supported by both its soft X-ray spectrum and its short-term X-ray variability which argues against a scattering/reflection dominated spectrum. We have also analyzed a recent 55 ks *NuSTAR* observation (observation ID 60101004002) of PHL 1811 following the basic procedure in Luo et al. (2014). There is a weak detection of this source in the 3–8 keV band, but no (or at most a marginal) detection in the 8–24 keV band, indicating that there is no strong Compton-reflection component emerging in its hard X-ray spectrum.

One promising method to identify intrinsically X-ray weak AGNs is to investigate the hard X-ray ( $\gtrsim 8$  keV) flux weakness and spectral shapes of candidate objects. In the hard X-ray band, due to the combined effects of photoelectric absorption and Compton scattering, a Compton-thick absorber usually results in a flat spectrum with a power-law photon index in a typical range of  $\Gamma \approx 0$ –1 (e.g., George & Fabian 1991; Comastri et al. 2011; Gandhi et al. 2014; Rovilos et al. 2014), while for radio-quiet type 1 quasars the mean  $\Gamma$  value

**Table 1**  
*Chandra* Observation Log and Target Properties

Object Name (LBQS B) (1)	Redshift (2)	$B_J$ (3)	Observation Star Date (4)	Observation ID (5)	New Exposure (ks) (6)	Combined Exposure (ks) (7)	$N_{\text{H,Gal}}$ ( $10^{20} \text{ cm}^{-2}$ ) (8)	BI ( $\text{km s}^{-1}$ ) (9)	C IV EW ( $\text{\AA}$ ) (10)	$v_{\text{max}}$ ( $\text{km s}^{-1}$ ) (11)	$R^*/R_i$ (12)
0021–0213	2.35	18.68	2009 Oct 30	8918	29.80	36.55	2.71	5179	40.20	20138	$< 0.11/\dots$
1203+1530	1.63	18.70	2016 Apr 22	17465	11.95	19.02	2.30	1517	25.40	11702	$\dots/< 0.67$
1212+1445	1.63	17.87	2016 Apr 13	17466	11.17	15.67	2.94	3618	38.80	19368	$0.01/< 0.34$
1235+1453	2.70	18.56	2016 May 2	17467	11.27	17.91	2.31	2657	19.30	14414	$< 0.42/< 0.27$
1442–0011	2.23	18.24	2016 May 18	17468	10.67	14.95	3.39	5142	39.10	22834	$-0.20/< 0.51$
1443+0141	2.45	18.20	2016 May 12	17469	10.08	16.02	3.51	7967	44.00	$> 25000$	$< 0.07/< 0.77$
2201–1834	1.81	17.81	2015 May 23	17470	8.60	13.69	2.54	1612	27.30	19682	$< -0.45/\dots$

**Note.** — Cols. (1)–(2): object name and redshift. Col. (3):  $B_J$ -band magnitude, adopted from Gallagher et al. (2006). Cols. (4)–(5): Start date and observation ID of the new *Chandra* archival observation (for LBQS 0021–0213) or Cycle 16 observation (for the other objects). Cols. (6)–(7): exposure time of the new observation and combined exposure time of the previous and new observations. Col. (8): Galactic neutral hydrogen column density (Dickey & Lockman 1990). Cols. (9)–(11): BALnicity Index, C IV absorption equivalent width, and maximum velocity of blueshifted C IV absorption, adopted from Gallagher et al. (2006). Col. (12): Logarithm of radio-to-optical flux ratio, adopted from Gallagher et al. (2006).  $R^*$  is the logarithm of the ratio between the flux densities at 5 GHz and 2500  $\text{\AA}$  (Stoake et al. 1992), and  $R_i$  is the logarithm of the ratio between the flux densities at 1.4 GHz and the SDSS  $i$  band (Ivezić et al. 2002). Objects with either  $R^*$  or  $R_i$  larger than 1 are considered to be radio loud.

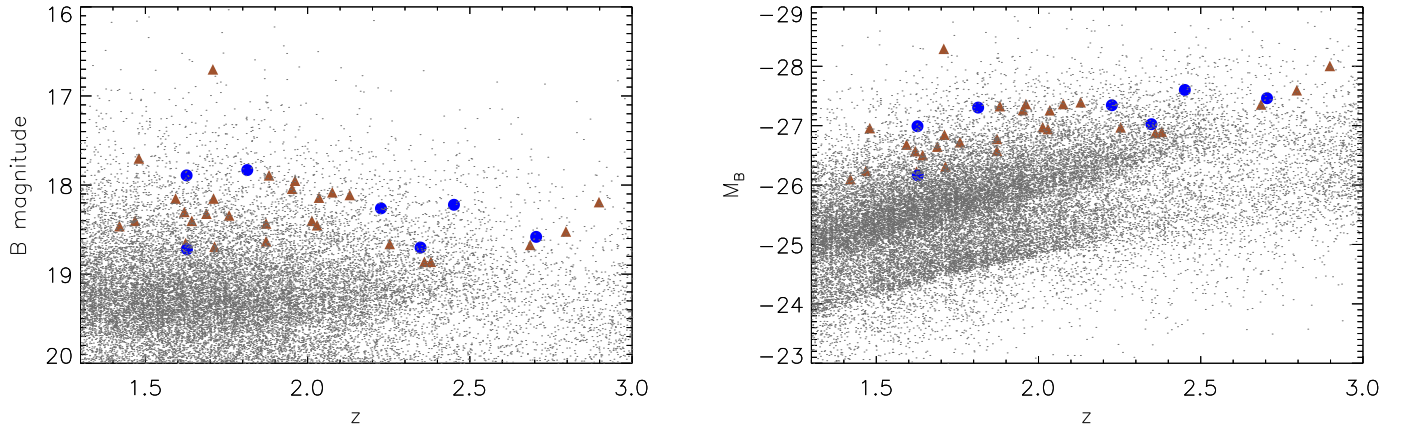


**Figure 2.** Redshift versus (a) apparent and (b) absolute  $B$ -band magnitudes for the 35 BAL quasars in Gallagher et al. (2006). Our subsample (7 objects) is shown as blue dots and the others are shown as brown triangles. The underlying small gray dots are objects from the SDSS DR7 quasar catalog (Schneider et al. 2010). The  $B$ -band magnitudes of the SDSS quasars and LBQS quasars were converted from the  $g$ -band and  $B_J$ -band magnitudes, respectively, assuming an optical power-law spectrum ( $f_\nu \propto \nu^\alpha$ ) with a slope of  $\alpha = -0.5$  (e.g., Vanden Berk et al. 2001).

is  $\approx 1.9$ – $2.0$  with an intrinsic dispersion of  $\sigma_\Gamma \approx 0.2$ – $0.3$  (e.g., Reeves et al. 1997; Just et al. 2007; Young et al. 2009; Mateos et al. 2010; Scott et al. 2011). Based on this consideration, *NuSTAR* observations were used to distinguish between the scenarios of Compton-thick absorption and intrinsic X-ray weakness, and a few candidates for intrinsically X-ray weak BAL quasars were found (Luo et al. 2013, 2014). Stacking analyses indicate that these objects have soft effective photon indices in the 3–24 keV band on average, disfavoring the Compton-thick absorption scenario.

At a redshift of  $z \approx 2$ , *Chandra* 0.5–8 keV observations sample rest-frame energies in the range  $\approx 1.5$ –24 keV, similar to the hard X-ray band probed by *NuSTAR*. Thus, *Chandra* observations of high-redshift targets can also be used to find intrinsically X-ray weak AGNs. The hard X-ray spectral shape can be described by the effective power-law photon index ( $\Gamma_{\text{eff}}$ ), derived from the ratio between the hard-band (2–8 keV, rest-frame  $\approx 6$ –24 keV) and soft-band (0.5–2 keV, rest-frame  $\approx 1.5$ –6 keV) count rates. Moreover, the hard X-ray flux weakness can be measured via comparing the hard-band derived  $\alpha_{\text{OX}}$  value ( $\alpha_{\text{OX,hard}}$ , with the rest-frame 2 keV flux density calculated from the observed hard-band flux assuming

$\Gamma = 2$ )<sup>10</sup> to the expectation ( $\alpha_{\text{OX,exp}}$ ) from the  $\alpha_{\text{OX}}$ – $L_{2500 \text{ \AA}}$  relation. If a  $z \approx 2$  AGN is significantly X-ray weak in the hard band and it also has a soft spectral shape from *Chandra* observations, it is a good candidate for being an intrinsically X-ray weak AGN.

Luo et al. (2013) applied the aforementioned method to search for intrinsically X-ray weak AGNs, using the *Chandra* photometric properties of the 35 LBQS BAL quasars in Gallagher et al. (2006). These BAL quasars have redshifts of  $z \approx 1.5$ –3. There are 23 sources that are detected in the hard band; they have either flat spectral shapes ( $\Gamma_{\text{eff}} < 1$ ) or  $\alpha_{\text{OX,hard}}$  values consistent with  $\alpha_{\text{OX,exp}}$ , indicating that these 23 sources are likely not intrinsically X-ray weak AGNs. Additionally, there are 12 hard-band undetected sources, including seven high-ionization BAL (HiBAL) quasars and five low-ionization (LoBAL) quasars.<sup>11</sup> Fig-

<sup>10</sup> Following Gallagher et al. (2006), we used  $\Gamma = 2$  instead of the measured  $\Gamma_{\text{eff}}$  to minimize the effect of potential absorption on the computation of  $f_{2\text{keV}}$  and  $\alpha_{\text{OX,hard}}$ .  $\Gamma \approx 2$  is the mean photon index for radio-quiet type 1 quasars.

<sup>11</sup> HiBAL quasars are objects showing only high-ionization BALs in UV spectra, and LoBAL quasars are objects showing strong Mg II or Al III BALs in UV spectra. Among the 35 BAL quasars in Gallagher et al. (2006), there are 24 HiBAL quasars, six LoBAL quasars, and five quasars with unknown

ure 1 shows a comparison of the soft-band flux weakness ( $\Delta\alpha_{\text{OX,soft}} = \alpha_{\text{OX,soft}} - \alpha_{\text{OX,exp}}$ ) to the hard-band flux weakness ( $\Delta\alpha_{\text{OX,hard}} = \alpha_{\text{OX,hard}} - \alpha_{\text{OX,exp}}$ ) for the 12 objects, where the soft-band derived  $\alpha_{\text{OX,soft}}$  is calculated using the soft-band flux and the measured  $\Gamma_{\text{eff}}$  value. The shaded regions ( $\Delta\alpha_{\text{OX}} = 0.3$ ) show the  $\approx 95\%$  ( $\approx 2\sigma$ ) uncertainties associated with  $\alpha_{\text{OX,exp}}$  (from Table 5 of Steffen et al. 2006). Since  $\alpha_{\text{OX,soft}}$  was computed using the measured  $\Gamma_{\text{eff}}$  value, and  $\alpha_{\text{OX,hard}}$  was calculated by assuming  $\Gamma = 2.0$ , consistent  $\Delta\alpha_{\text{OX,soft}}$  and  $\Delta\alpha_{\text{OX,hard}}$  values indicate  $\Gamma_{\text{eff}} \approx 2$  (a steep/soft spectral shape; slanted line in Figure 1). The 12 hard-band undetected objects only have upper limits on  $\Delta\alpha_{\text{OX,hard}}$ , and their hard-band flux weakness and effective photon indices cannot be constrained individually. Stacking analyses of the 12 sources were used to constrain their average X-ray properties. Stacked flux from the seven HiBAL quasars is significantly detected in both the soft and hard bands, while stacked flux from the five LoBAL quasars is only detected in the soft band. In Figure 1, the data points for the stacked sources are shown as stars. The stacked source of the seven HiBAL quasars lies outside the shaded regions (negative  $\Delta\alpha_{\text{OX,soft}}$  and  $\Delta\alpha_{\text{OX,hard}}$ ) and close to the slanted line, showing substantial hard-band flux weakness and a soft spectral shape with  $\Gamma_{\text{eff}} = 1.8^{+0.5}_{-0.5}$ . Thus, this stacked source is likely intrinsically X-ray weak, which suggests the presence of intrinsically X-ray weak AGNs among the seven HiBAL quasars. For the stacked source of the five LoBAL quasars, the spectral shape cannot be constrained due to the nondetection in the hard band. We used the Bayesian code BEHR (Park et al. 2006) to obtain a best-guess estimate of the effective photon index (see Section 4.4 of Luo et al. 2017), which is  $\Gamma_{\text{eff}} \approx 1.8$ . Given this estimated  $\Gamma_{\text{eff}}$  and the hard-band flux weakness, the stacked source of the five LoBAL quasars is perhaps also intrinsically X-ray weak.

In order to identify intrinsically X-ray weak AGNs individually and improve the constraints upon the fraction of such objects among BAL quasars, we analyzed additional *Chandra* observations for the seven HiBAL quasars. The HiBAL quasars are the majority population of BAL quasars, and they are also more amenable to economical *Chandra* observations than the LoBAL quasars; thus we focus upon the seven HiBAL quasars in this study. One object (LBQS 0021–0213) was serendipitously detected (3.8' away from the observation aim point) in a new *Chandra* archival observation (Cycle 9, observation ID 8918) in addition to the observation in Gallagher et al. (2006), and it was observed with the I-array of the Advanced CCD Imaging Spectrometer (ACIS, Garmire et al. 2003) for a 29.8 ks exposure. The other six objects have our new *Chandra* observations in Cycle 16, and they were observed using the S3 CCD of ACIS with  $\approx 10$  ks exposures. The details of the *Chandra* observations for the seven objects are listed in Table 1. Table 1 also includes the BAL properties of these objects adopted from Gallagher et al. (2006). The redshift versus apparent and absolute *B*-band magnitude distributions for the 35 BAL quasars in the Gallagher et al. (2006) sample (including our subsample of the seven quasars) and objects from the SDSS DR7 quasar catalog (Schneider et al. 2010) are shown in Figure 2. Our targets are among the most luminous quasars in the optical/UV. Their high luminosities and redshifts make them

BAL types, for which the available UV spectra do not cover the Mg II region. HiBAL quasars are the majority population ( $\approx 85\%$ ) of BAL quasars (e.g., Weymann et al. 1991; Sprayberry & Foltz 1992), and thus we consider the two objects with unknown BAL types among the 12 hard-band undetected objects as HiBAL quasars.

more representative of the typically studied BAL-quasar population than the generally low-luminosity and low-redshift objects amenable to observations with *NuSTAR*.

### 3. X-RAY DATA ANALYSIS

Each of our seven sample objects has two *Chandra* observations. We analyzed the observational data using the *Chandra* Interactive Analysis of Observations (CIAO; v4.9) tools. For each observation, we ran the CHANDRA\_REPRO script to generate a new level 2 event file, and we filtered background flares by running the DEFLARE script with an iterative  $3\sigma$  clipping algorithm. The images in the full (0.5–8 keV), soft (0.5–2 keV), and hard (2–8 keV) bands were constructed by running a DMCPY script. To detect corresponding X-ray sources for our sample objects and search for other sources, we used the automated source-detection tool WAVDETECT (Freeman et al. 2002) with a false-positive probability threshold of  $10^{-6}$  and wavelet scale sizes of 1, 1.414, 2, 2.828, 4, 5.656, and 8 pixels. Each source is detected in at least one of the two observations, which contains an X-ray point source at a location consistent with the optical position of the target. The measured X-ray-to-optical positional offsets of the objects span a range of  $0.2''$ – $2.0''$  with a mean value of  $0.8''$ .

We extracted source counts in the three energy bands with aperture photometry. The source-extraction region is a circular aperture centered on the X-ray position<sup>12</sup> with a  $2''$  radius. For the on-axis observations, the encircled-energy fractions (EEFs) for the source aperture are 0.939, 0.959, and 0.907 in the full, soft, and hard bands, respectively. For LBQS 0021–0213 in the second observation with an off-axis angle of  $3.8'$ , the EEFs are 0.812, 0.834, 0.760 in the full, soft, and hard bands, respectively. The background was estimated over an annulus centered on the same position with a  $10''$  inner radius and a  $40''$  outer radius. There are no X-ray sources in the background region for any observation. For each band of each source, we summed the extracted counts from the source-extraction regions of the previous and new observations, to obtain the total source counts ( $S$ ). Similarly, the total background counts ( $B$ ) were the sum of the extracted counts from the background annulus of the two observations. The  $1\sigma$  errors on the extracted source and background counts were derived following the Poisson approach of Gehrels (1986). The net counts were obtained by subtracting from the source counts the estimated number of background counts in the source aperture, which was scaled from the total background counts with a scaling factor (*BACKSCAL*) being the ratio between the areas of the background and the source-extraction regions.

We then calculated a binomial no-source probability,  $P_B$ , to assess the significance of the source signal (e.g., Broos et al. 2007; Xue et al. 2011; Luo et al. 2013, 2015), which is defined as

$$P_B = \sum_{x=S}^N \frac{N!}{x!(N-x)!} p^x (1-p)^{N-x}, \quad (1)$$

where  $N = S + B$  and  $p = 1/(1 + \text{BACKSCAL})$ .  $P_B$  represents the probability of observing  $\geq S$  counts in the source-extraction

<sup>12</sup> LBQS 1212+1445 and LBQS 2201–1834 are detected only in one of the two observations, and the measured X-ray-to-optical positional offsets are  $0.6''$  and  $1.1''$ , respectively. For each of the two sources, we adopted its detected X-ray position in both observations to extract X-ray photometry. The results do not change if we adopt their optical positions to extract X-ray photometry.



region under the assumption that there is no real source at the relevant location. A smaller  $P_B$  value indicates a more significant signal. If the measured  $P_B$  value in a given band is smaller than a given threshold, we considered the source detected in this band, and provided measurements of the photometric properties; otherwise we provided upper-limit constraints. We adopted a  $P_B$  threshold of 0.04 (corresponding to a  $\approx 2.1\sigma$  significance level in a Gaussian distribution), which is appropriate for extracting X-ray photometry of sources at pre-specified positions (e.g., Luo et al. 2014, 2015). Given this threshold, we expect only 0.28 false detections ( $P_B < 0.04$  caused by background fluctuations) in a given band for seven trials/targets. Four of the seven targets are significantly ( $> 4\sigma$ ) detected in both the soft and hard bands. Two targets (LBQS 1203+1530 and LBQS 1442-0011) are significantly ( $> 4\sigma$ ) detected in the soft band, while they are weakly detected in the hard band with  $P_B$  values of 0.033 and 0.019, respectively. These relatively weak signals are reflected in the large uncertainties on their hard-band counts. The other target (LBQS 2201-1834) is undetected in both the soft and hard bands. For the detected sources, we provided net-count measurements along with their  $1\sigma$  errors; the errors were derived from the  $1\sigma$  errors on the extracted source and background counts, using the formula for the propagation of uncertainties (as in, e.g., Section 1.7.3 of Lyons 1991). For the undetected source, we derived 90% confidence-level upper limits on the source counts using the Bayesian approach of Kraft et al. (1991). The source counts or their upper limits in the soft and hard bands are listed in Table 2.

The effective photon index ( $\Gamma_{\text{eff}}$ ) for a power-law spectrum was derived from the observed band ratio, which is defined as the ratio between the soft-band and the hard-band counts. The procedure is as follows: (1) for each observation, we generated a set of mock spectra using the FAKEIT routine in XSPEC (v12.9.1; Arnaud 1996) and the spectral response files, assuming a set of  $\Gamma$  values for a power-law model that is modified by Galactic absorption (e.g., Gallagher et al. 2006; Luo et al. 2017); (2) we then computed the corresponding set of band ratios from the simulated spectra; (3) the results from the two observations of each source were combined by calculating the exposure-time weighted means of the two sets of band ratios; (4) the effective photon index was then derived from the observed band ratio by a simple interpolation of the  $\Gamma$ -band ratio pairs. We used BEHR to derive the  $1\sigma$  errors on the band ratios. The errors on  $\Gamma_{\text{eff}}$  were propagated from the errors on the band ratios.

We also used XSPEC to fit the target spectra. For each observation, the source spectrum was extracted from a circular region centered on the X-ray position with a radius of  $3''$  for the on-axis objects or a radius of  $4''$  for the off-axis object (LBQS 0021-0213 in the second observation). The background spectrum was extracted from an annulus centered on the same position with a  $10''$  inner radius and a  $40''$  outer radius. For each source, we combined the spectra of two observations. We used the C-statistic and a power-law model modified by Galactic absorption (WABS\*ZPOWERLW) to fit the 0.5–8 keV combined spectrum. Only spectra with more than 4 counts are useful, and thus we did not fit the spectrum of LBQS 2201-1834. The total numbers of counts in the combined spectra of the other targets span a range of 7–34. The best-fit  $\Gamma_{\text{XSPEC}}$  values and their  $1\sigma$  errors are listed in column 6 of Table 2. These  $\Gamma_{\text{XSPEC}}$  values are in general consistent with the  $\Gamma_{\text{eff}}$  values, considering their large uncertainties. In the following analyses and discussions, we adopted

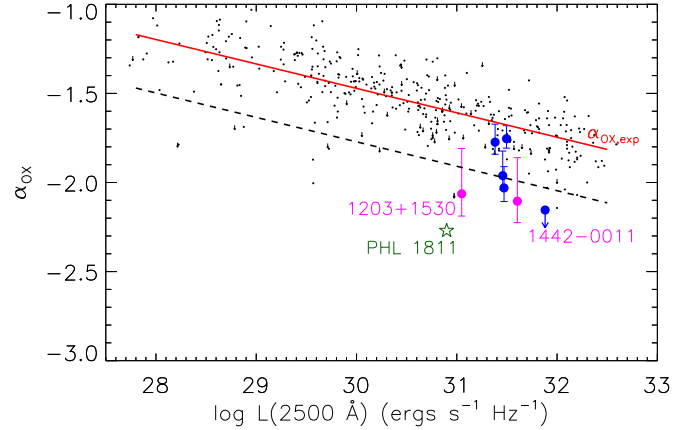


**Figure 3.** X-ray-to-optical power-law slope ( $\alpha_{\text{OX}}$ ) vs. 2500 Å monochromatic luminosity for our seven sample objects (LBQS 1203+1530 and LBQS 1442-0011 in magenta and the others in blue). The small black dots and downward arrows (upper limits) are for the typical AGN samples in Steffen et al. (2006), and the solid red line shows the  $\alpha_{\text{OX}}-L_{2500}$  relation. PHL 1811 is shown as a green star. For our sample objects, the y-axis values ( $\alpha_{\text{OX}}$ ) were computed using the hard-band fluxes and  $\Gamma = 2$ . Objects lying below the dashed line ( $\Delta\alpha_{\text{OX}} = -0.3$ ) show significant hard-band flux weakness.

the  $\Gamma_{\text{eff}}$  values; using  $\Gamma_{\text{XSPEC}}$  instead would not change our results.

We converted the observed source count rates to fluxes using a power-law spectrum model with a photon index of  $\Gamma_{\text{eff}}$  and the spectral response files. The errors on the fluxes or flux densities were propagated from the errors on the net counts. We used the measured  $\Gamma_{\text{eff}}$  value and the soft-band flux to derive a 2 keV flux density ( $f_{2\text{keV,soft}}$ ), and computed the soft-band derived optical-to-X-ray slope ( $\alpha_{\text{OX,soft}}$ ). Additionally, we used  $\Gamma = 2$  and the hard-band flux to calculate a hard-band derived 2 keV flux density ( $f_{2\text{keV,hard}}$ ), and computed the hard-band derived  $\alpha_{\text{OX,hard}}$  (see Footnote 10). The flux density at rest-frame 2500 Å ( $f_{2500\text{Å}}$ ) and the 2500 Å monochromatic luminosity ( $L_{2500\text{Å}}$ ) used to compute  $\alpha_{\text{OX,soft}}$  and  $\alpha_{\text{OX,hard}}$  were adopted from Gallagher et al. (2006). The errors of  $\alpha_{\text{OX,soft}}$  ( $\alpha_{\text{OX,hard}}$ ) were propagated from the errors of  $f_{2\text{keV,soft}}$  ( $f_{2\text{keV,hard}}$ ). For the one undetected source (LBQS 2201-1834), we assumed  $\Gamma_{\text{eff}} = 1$  to calculate the upper limits on fluxes and  $f_{2\text{keV,soft}}$  (and subsequently  $\alpha_{\text{OX,soft}}$ ) because of its BAL-quasar nature, which suggests a hard spectrum due to absorption (e.g., Gallagher et al. 2006). We used  $\Gamma = 2$  and the hard-band flux upper limit to calculate the upper limit on  $f_{2\text{keV,hard}}$  (and subsequently  $\alpha_{\text{OX,hard}}$ ). In Table 2, we list the band ratio,  $\Gamma_{\text{eff}}$ , and flux values for our sample objects. The other X-ray properties are listed in Table 3.

#### 4. TWO GOOD CANDIDATES FOR INTRINSICALLY X-RAY WEAK AGNS

The seven sample objects were undetected in the hard band (2–8 keV,  $\approx 6$ –24 keV in the rest frame) in the previous 5–7 ks *Chandra* observations of Gallagher et al. (2006). After combining the data from previous and new observations, the exposure times reach 13.6–36.6 ks. Except for one object (LBQS 2201-1834) that is still undetected in the hard band, four objects are now significantly ( $> 3\sigma$ ) detected, and the other two objects (LBQS 1203+1530 and LBQS 1442-0011) are weakly detected ( $2.1\sigma$  and  $2.3\sigma$ , respectively). Half of the six detected objects show hard X-ray spectral shapes with  $\Gamma_{\text{eff}}$  values in the range of 0.4–1.1

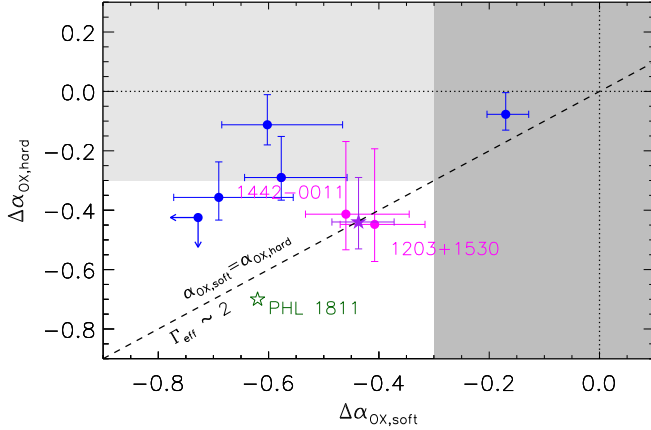


**Figure 4.** An updated version of Figure 1, showing  $\Delta\alpha_{\text{OX,hard}}$  versus  $\Delta\alpha_{\text{OX,soft}}$  for our seven sample objects (blue and magenta data points) and PHL 1811 (green star) after considering the new observations. LBQS 1203+1530 and LBQS 1442-0011 are shown as magenta data points, and the stacked source of these two objects is shown as a purple star. For the detected objects, the uncertainties of  $\Delta\alpha_{\text{OX,hard}}$  ( $\Delta\alpha_{\text{OX,soft}}$ ) are shown. For the single object (LBQS 2201-1834) that is undetected in both the soft and hard bands, upper limits on  $\Delta\alpha_{\text{OX,hard}}$  ( $\Delta\alpha_{\text{OX,soft}}$ ) are shown as arrows. The dark and light shaded regions show the  $\approx 95\%$  ( $\approx 2\sigma$ ) confidence-level uncertainties of  $\alpha_{\text{OX,exp}}$ . The slanted dashed line indicates  $\alpha_{\text{OX,soft}} = \alpha_{\text{OX,hard}}$  and  $\Gamma_{\text{eff}} \approx 2$ . Objects lying outside the shaded regions are significantly X-ray weak, and objects lying near the slanted line have soft spectra.

( $-0.4$ – $1.5$  according to the  $1\sigma$  uncertainties). The others (including LBQS 1203+1530 and LBQS 1442-0011) show soft X-ray spectral shapes with  $\Gamma_{\text{eff}} > 1.7$ .

Figure 3 shows the  $\alpha_{\text{OX}}$  versus  $L_{2500\text{Å}}$  distribution for our seven sample objects, PHL 1811, and the typical AGN samples in Steffen et al. (2006). For our sample objects, we used the hard-band derived  $\alpha_{\text{OX,hard}}$  values. We considered  $\Delta\alpha_{\text{OX,hard}} < -0.3$  (corresponding to a hard-band flux weakness factor<sup>13</sup> of  $f_{\text{weak}} > 6$ ) as the criterion for a object being X-ray weak (see Section 2), indicated by the dashed line in Figure 3. Four objects in our sample (including the undetected object) meet this criterion, showing significant hard-band flux weakness.

We applied the method introduced in Section 2 to identify intrinsically X-ray weak AGNs in our sample. Similar to Figure 1, Figure 4 shows a comparison of the soft-band flux weakness ( $\Delta\alpha_{\text{OX,soft}}$ ) to the hard-band flux weakness ( $\Delta\alpha_{\text{OX,hard}}$ ) for the seven sample objects. Compared to Figure 1, the hard-band flux weakness of six objects can be constrained now. In particular, two sources (LBQS 1203+1530 and LBQS 1442-0011, magenta points in Figures 3 and 4) lie outside the shaded regions and close to the slanted line, showing significant hard-band flux weakness and soft spectral shapes. For LBQS 1203+1530 (LBQS 1442-0011), the effective power-law photon index is  $\Gamma_{\text{eff}} = 2.2^{+0.9}_{-0.9}$  ( $\Gamma_{\text{eff}} = 1.9^{+0.9}_{-0.8}$ ), and the factor of hard-band flux weakness ( $f_{\text{weak}}$ ) is 14.7 (11.9). Therefore, we suggest that these two sources are good candidates for intrinsically X-ray weak AGNs. We note that due to limited photon statistics, there are substantial uncertainties on the derived effective photon indices and factors of hard-band flux weakness for LBQS 1203+1530 and LBQS 1442-0011; e.g., their  $\alpha_{\text{OX,hard}}$  error bars extend beyond the  $\Delta\alpha_{\text{OX}} = -0.3$  line in Figure 3, and the upper boundaries correspond to  $f_{\text{weak}}$  of only 3.2 and 2.8, respectively.

<sup>13</sup> It is calculated as  $f_{\text{weak}} = 10^{-\Delta\alpha_{\text{OX,hard}}/0.3838}$ .

Deeper observations are needed to constrain better their spectral shapes and hard-band flux weakness, and confirm their intrinsically X-ray weak nature.

We also stacked the X-ray emission of LBQS 1203+1530 and LBQS 1442-0011, aiming to obtain a more significant detection and constrain their average X-ray properties. Indeed, the stacked source is significantly ( $3.1\sigma$ ) detected in the hard band, and it also has significant hard-band flux weakness ( $f_{\text{weak}} = 14.0$ ) and a soft spectral shape ( $\Gamma_{\text{eff}} = 2.1^{+0.6}_{-0.6}$ ). The stacked source is shown as a purple star in Figure 4, which has smaller errors of  $\Delta\alpha_{\text{OX,soft}}$  and  $\Delta\alpha_{\text{OX,hard}}$  compared to the two objects individually.

One of the seven targets, LBQS 2201-2834, remains undetected in the soft and hard bands. It is significantly X-ray weak in the hard band ( $f_{\text{weak}} > 12.8$ ), but we cannot constrain its spectral shape due to the nondetection. It could still be an intrinsically X-ray weak AGN, and a deeper X-ray observation is required to determine its nature.

#### 4.1. Fraction of Intrinsically X-ray Weak BAL Quasars

The Gallagher et al. (2006) LBQS BAL quasars are the only well-defined BAL-quasar sample that has been investigated systematically for the presence of intrinsically X-ray weak AGNs. With the two good candidates identified in this study, we can constrain the fraction of intrinsically X-ray weak AGNs. In addition to our seven sample objects, the other 22 objects among the 29 HiBAL quasars in Gallagher et al. (2006) do not show evidence of intrinsic X-ray weakness (see Section 4.2.3 of Luo et al. 2013). Since the undetected source in our sample (LBQS 2201-1834) could still be a candidate intrinsically X-ray weak AGN, we consider there to be 2-3 candidates for intrinsically X-ray weak AGNs. We have thus constrained the fraction of intrinsically X-ray weak AGNs among HiBAL quasars to be  $\approx 7^{+8}_{-2} - 10^{+9}_{-3}\%$  ( $2/29$ – $3/29$ ); the  $1\sigma$  Poisson uncertainties were computed following the approach in Cameron (2011).

In addition to the 29 HiBAL quasars, there are six LoBAL quasars in the sample of Gallagher et al. (2006). Five of the six LoBAL quasars are undetected in the hard band, and the stacked upper limit in Figure 1 suggests the presence of intrinsically X-ray weak AGNs among these five objects (see also Section 2). There is probably a substantial fraction of intrinsically X-ray weak AGNs among the five hard-band undetected LoBAL quasars based on the following considerations: (1) Among the 29 HiBAL quasars, the three candidates for intrinsically X-ray weak AGNs (LBQS 1203+1530, LBQS 1442-0011, and LBQS 2201-1834) are the X-ray weakest in the hard band (see Figure 9 of Luo et al. 2013 and Figure 4); (2) Probably intrinsically X-ray weak BAL quasars tend to be X-ray weaker than X-ray absorbed BAL quasars; (3) Given the individual and stacked upper limits on  $\Delta\alpha_{\text{OX,hard}}$  of the five hard-band undetected LoBAL quasars, they appear to be X-ray weaker than the HiBAL quasars in general (Figure 1). Therefore, it is probable that the fraction of intrinsically X-ray weak AGNs among LoBAL quasars is larger than that in HiBAL quasars. If all the five hard-band undetected LoBAL quasars are intrinsically X-ray weak, there would be up to 8 intrinsically X-ray weak AGNs among the 35 BAL quasars in Gallagher et al. (2006). Therefore, the fraction of intrinsically X-ray weak AGNs among the entire BAL quasar population (both HiBAL and LoBAL quasars) is  $\approx 6^{+6}_{-2} - 23^{+8}_{-6}\%$  ( $2/35$ – $8/35$ ). This is a more robust constraint compared to the  $\approx 17$ – $40\%$  fraction suggested in Luo et al.

(2013), which was estimated solely from the stacking analyses.

## 5. DISCUSSION

As discussed in Section 2, a soft spectrum in the hard X-ray ( $\gtrsim 8$  keV) band indicated by a steep effective power-law photon index can rule out the general Compton-thick absorption scenario. However, there exists an alternative Compton-thick scenario with an exceptional geometrical configuration (e.g., Murphy & Yaqoob 2009; Matt et al. 2012; Bianchi et al. 2017). In this scenario, there is a very compact neutral Compton-thick absorber with an extremely high column density ( $N_H \gtrsim 10^{25} \text{cm}^{-2}$ ) along the line of sight. The intrinsic emission along the line-of-sight is completely absorbed up to very high energies, and there is hardly any Compton-reflection hump emerging in the spectrum due to the very small covering factor of the neutral absorber to the X-ray corona. Thus the observed spectrum is dominated by a soft reflected component from a large-scale highly ionized "mirror" up to hard X-rays ( $\approx 8\text{--}20$  keV). The scenario requires a rather peculiar and finely tuned configuration, and there have been no such objects discovered before, and thus we acknowledge such a possibility, but consider it unlikely.

We constructed rest-frame infrared (IR) to X-ray spectral energy distributions (SEDs) for our seven sample objects, as shown in Figure 5. The IR-to-UV photometric data were gathered from the public catalogs of Multiband Imaging Photometer for *Spitzer* (MIPS; Rieke et al. 2004), *Wide-field Infrared Survey Explorer* (WISE; Wright et al. 2010), Two Micron All Sky Survey (2MASS; Skrutskie et al. 2006), Sloan Digital Sky Survey (SDSS; York et al. 2000), and *Galaxy Evolution Explorer* (GALEX; Martin et al. 2005). The optical and UV data have been corrected for Galactic extinction following the dereddening approach of Cardelli et al. (1989) and O'Donnell (1994). We also used the  $B_J$ -band magnitude adopted from Gallagher et al. (2006) and the 2 keV and 10 keV luminosities, which were derived from the soft and hard bands, respectively, by assuming a power-law model with measured  $\Gamma_{\text{eff}}$ . These SEDs are in general consistent with those presented in Gallagher et al. (2007). For comparison, the composite SED of typical SDSS quasars in Richards et al. (2006) is also shown in Figure 5. Most of the mid-infrared-to-UV SEDs of these objects are generally consistent with those of typical quasars, except for one peculiar object (LBQS 1212+1445), which shows unusually weak mid-infrared-to-near-infrared emission (see the WISE data points in the corresponding panel of Figure 5), suggesting that it could be a "hot-dust-poor quasar" (e.g., Jiang et al. 2010; Hao et al. 2011; Lyu et al. 2017). Compared to typical quasars, LBQS 1203+1530 and LBQS 1442–0011 have weak X-ray emission, and the two X-ray data points of these two objects also indicate a steep spectral shape ( $\Gamma \approx 2$ ) that is typical of type 1 quasars.

We have estimated that the fraction of intrinsically X-ray weak AGNs among BAL quasars is  $\approx 6^{+6}_{-2}\text{--}23^{+8}_{-6}\%$ . This fraction appears considerably larger than the  $\lesssim 2\%$  fraction among non-BAL quasars (e.g., Gibson et al. 2008). One possible interpretation of this significant difference is that disk winds in intrinsically X-ray weak BAL quasars can be launched easily with larger covering factors of the nuclei, as the line-driven winds are not significantly ionized by the nuclear X-ray emission; thus intrinsically X-ray weak quasars would be preferentially observed as BAL quasars (e.g., Luo et al. 2013). We investigate whether

LBQS 1203+1530 and LBQS 1442–0011 show obviously stronger outflowing winds, by comparing their BALnicity Indices (BI; the modified equivalent width of the BAL as defined in Weymann et al. 1991) and maximum velocities of C IV absorption blueshift ( $v_{\text{max}}$ ) to those of the other HiBAL quasars in Gallagher et al. (2006). The distributions of the two parameters are shown in Figure 6. LBQS 1442–0011 shows relatively large BI and  $v_{\text{max}}$  values among these HiBAL quasars, but LBQS 1203+1530 does not show these characteristics. It is probable that the two parameters alone are not good indicators of wind strength due to the complication from the orientation effect. Another interpretation is that disk winds in intrinsically X-ray weak BAL quasars are not necessarily extremely strong (with high column densities and/or large velocities) but just have large covering factors.

We could also estimate the frequency of intrinsically X-ray weak AGNs among the general type 1 quasar population and assess its effect on X-ray surveys for AGN census work. The fraction of intrinsically X-ray weak AGNs among HiBAL quasars that we constrained is  $\approx 7\text{--}10\%$ , and the fraction of intrinsically X-ray weak AGNs among BAL quasars could be up to  $\approx 23\%$  (see Section 4.1). Since the subclass of BAL quasars is thought to account for  $\approx 15\%$  of quasars (e.g., Hewett & Foltz 2003; Reichard et al. 2003; Gibson et al. 2009; Trump et al. 2006; Allen et al. 2011), the fraction of intrinsically X-ray weak BAL quasars among the general quasar population should be  $\lesssim 3.5\%$ . In addition, the fraction of intrinsically X-ray weak AGNs among non-BAL quasars is  $\lesssim 2\%$  (Gibson et al. 2008), which translates to a  $\lesssim 1.7\%$  fraction among the general type 1 quasar population. In total, intrinsically X-ray weak AGNs likely comprise a small minority ( $\lesssim 5.2\%$ ) of the luminous type 1 AGN population, and they should not affect significantly the completeness of these AGNs found in deep X-ray surveys. This is consistent with AGN selection results for sensitive multiwavelength survey fields (e.g., Brandt & Alexander 2015).

The underlying physics responsible for the intrinsically weak X-ray emission remains unclear. It could be related to some process that quenches the coronal X-ray emission (Proga 2005; Leighly et al. 2007b; Luo et al. 2013). Another possible scenario is that intrinsic X-ray weakness is related to a very high accretion rate of the accretion flow (e.g., Leighly et al. 2007b; Luo et al. 2014), where the accretion timescale is shorter than the diffusion timescale of X-ray photons that are produced close to the BH. We thus searched for Eddington-ratio estimates ( $L/L_{\text{Edd}}$ ) for the 29 HiBAL quasars in Gallagher et al. (2006) from the literature, and 19 of them have such estimates from Yuan & Wills (2003), Dietrich et al. (2009) and Shen et al. (2011). LBQS 1442–0011 and LBQS 1203+1530 do not show high Eddington ratios (0.25 and 0.17, respectively) relative to the other HiBAL quasars with Eddington ratios in the range of 0.14–1.47. However, there are only six sources (including LBQS 1442–0011) with BH-mass estimates based on the  $H\beta$  line profile using the single-epoch virial mass approach, and the other objects (including LBQS 1203+1530) have only Mg II- or C IV-based BH-mass estimates (Shen et al. 2011), that are less reliable or even systematically in error. Additional near-IR spectra are required to provide more reliable  $H\beta$ -based estimates of BH masses and Eddington ratios, and assess if intrinsic X-ray weakness is related to very high accretion rates.

## 6. SUMMARY AND FUTURE WORK

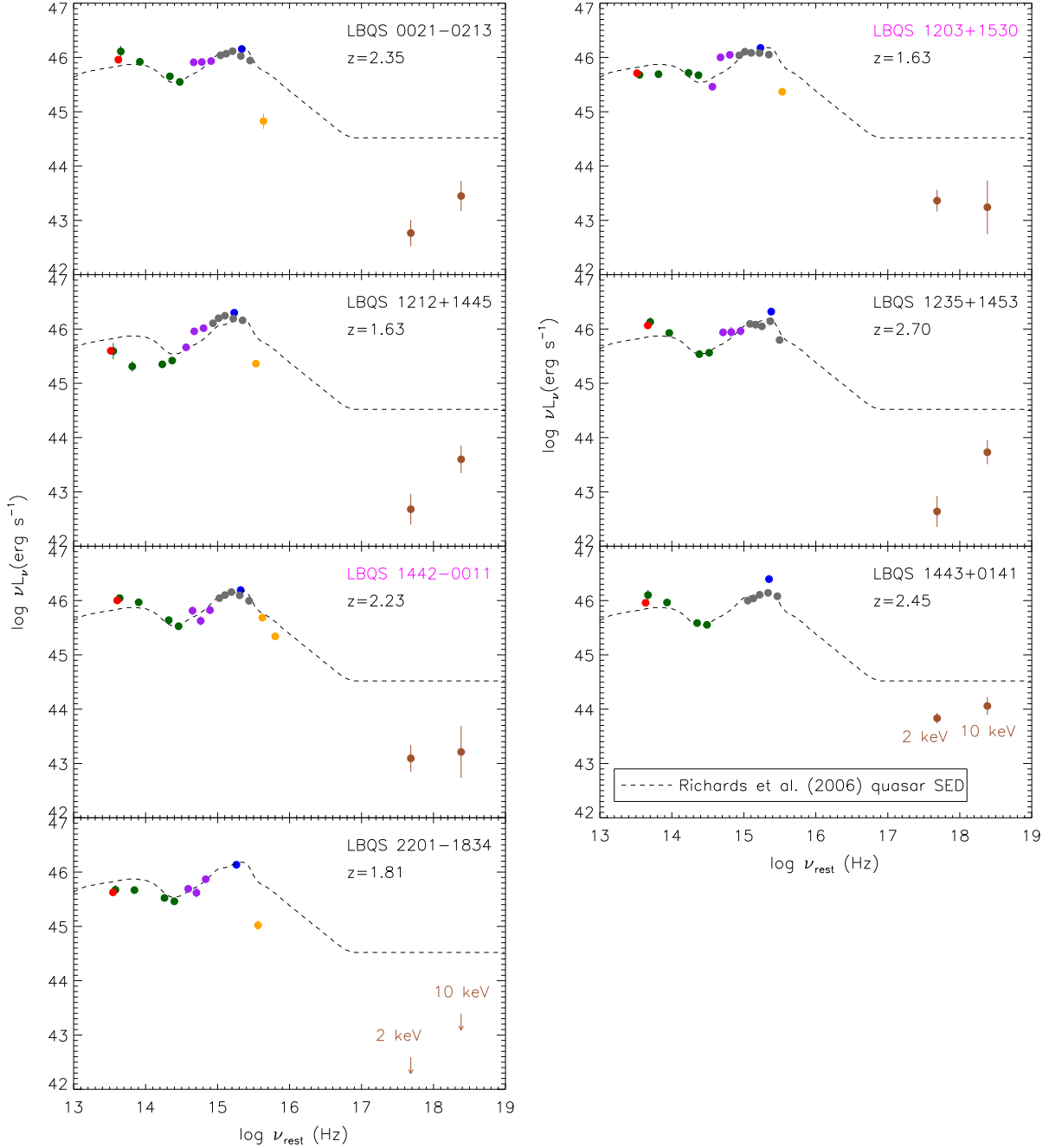


**Figure 5.** Rest-frame IR-to-X-ray SEDs for the seven sample objects. The IR-to-UV photometric data points were gathered from *Spitzer* MIPS (24  $\mu$ m, red), *WISE* (green), 2MASS (purple), SDSS (gray), LBQS (blue), and *GALEX* (orange) catalogs. The 2 keV and 10 keV data of *Chandra* (brown points and arrows) were derived from 0.5–2 keV and 2–8 keV fluxes (or flux upper limits), respectively. The SED for each object was scaled to the composite quasar SED of optically luminous SDSS quasars (Richards et al. 2006) at rest-frame 1  $\mu$ m. The object names (LBQS 1203+1530 and LBQS 1442–0011) of our two good candidates for intrinsically X-ray weak AGNs are highlighted in magenta. These multi-band observations are non-simultaneous, and thus the SEDs may be affected by variability.

In this paper, we have analyzed the combined  $\approx 14$ –37 ks *Chandra* data of seven hard-band undetected optically bright HiBAL quasars from Gallagher et al. (2006). Except for one target that is still undetected, the other six targets are now detected in the hard band. We constrained their hard-band (rest-frame  $\approx 6$ –24 keV) flux weakness and effective power-law photon indices, and found that two targets (LBQS 1203+1530 and LBQS 1442–0011) show soft spectral shapes ( $\Gamma_{\text{eff}} = 2.2^{+0.9}_{-0.9}$  and  $1.9^{+0.9}_{-0.8}$ ) and significant

hard-band flux weakness (by factors of 14.7 and 11.9), suggestive of being good candidates for intrinsically X-ray weak BAL quasars. These two objects are among the best candidates for intrinsically X-ray weak AGNs besides PHL 1811.

The 35 LBQS BAL quasars in Gallagher et al. (2006) are the only well-defined BAL-quasar sample that has been investigated systematically for the presence of intrinsically X-ray weak AGNs. Combined with the results of Luo et al. (2013), we constrained the fraction of intrinsically X-ray weak AGNs



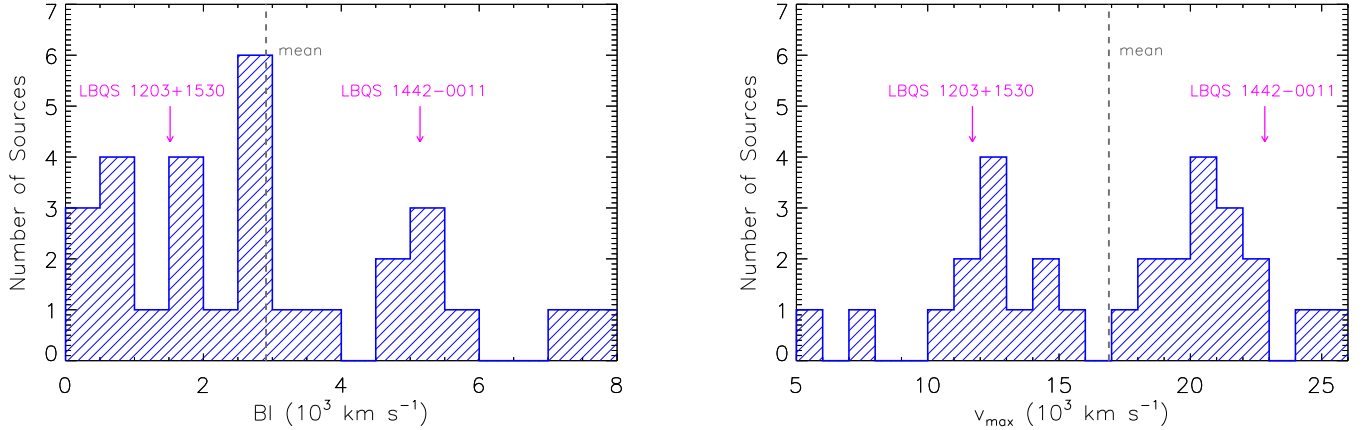


**Figure 6.** Distribution of (a) BALnicity index (BI) and (b) maximum velocity of C IV absorption blueshift ( $v_{\max}$ ) for the 29 HiBAL quasars in the Gallagher et al. (2006) sample (blue histogram). The vertical dashed line marks the mean value of each parameter for the 29 objects. The magenta arrows indicate BI and  $v_{\max}$  values for LBQS 1203+1530 and LBQS 1442-0011.

among HiBAL quasars to be  $\approx 7\text{--}10\%$  (2/29–3/29). Since the five hard-band undetected LoBAL quasars in Gallagher et al. (2006) could still be intrinsically X-ray weak, the fraction of intrinsically X-ray weak AGNs among the full BAL quasar population could be  $\approx 6\text{--}23\%$  (2/35–8/35). This fraction is considerably larger than the fraction ( $\lesssim 2\%$ ) of intrinsically X-ray weak AGNs among non-BAL quasars, suggesting that intrinsically X-ray weak AGNs are preferentially observed as BAL quasars, probably related to winds launched by accretion disks with larger covering factors of the nuclei.

Based on the current *Chandra* observational data, LBQS 1203+1530 and LBQS 1442-0011 are only weakly detected in the hard band. In both cases, there are only two counts in the source apertures, and the binomial no-source probabilities are  $P_B \approx 0.033$  and  $0.019$  (corresponding to  $2.1\sigma$  and  $2.3\sigma$  detections) for LBQS 1203+1530 and LBQS 1442-0011, respectively. Thus, there are considerable uncertainties on the effective power-law photon indices ( $\Gamma_{\text{eff}}$ ) and the factors of hard-band X-ray weakness ( $f_{\text{weak}}$ ), as shown in Figure 4, Table 2, and Table 3. Additional *Chandra* or *XMM-Newton* observations are required in order to improve the detection significance, better constrain the spectral shapes and hard-band flux weakness, and confirm the nature of these two objects as intrinsically X-ray weak AGNs. Moreover, LBQS 2201-1834 is still undetected in the soft and hard bands. A deeper X-ray observation is required to constrain its X-ray spectral shape and determine if it is an intrinsically X-ray weak AGN. This will also help to better constrain the fraction of intrinsically X-ray weak BAL quasars.

It will also be valuable if deeper observations are performed for the five hard-band undetected LoBAL quasars in Gallagher et al. (2006) to obtain hard-band detections and constrain their nature. These five LoBAL quasars probably host a larger fraction of intrinsically X-ray weak AGNs. However, given their significant X-ray weakness, such observations would be more expensive than those for the HiBAL quasars here. For example, given the photometric properties for the stacked source of the five LoBAL quasars (see Section 2 and Figure 1), we estimate that the total *Chandra* exposure time required to obtain a hard-band detection is  $\approx 44$  ks on average. Therefore, in order to detect all five LoBAL quasars individually, we would need to obtain a  $\gtrsim 40$  ks *Chandra* observation for each object in addition to its current  $\approx 5$  ks

*Chandra* exposure.

We thank the referee for reviewing the manuscript carefully and providing helpful comments. We thank Yong Shi, Qiusheng Gu, Peng Wei, Chen Hu, and Pu Du for helpful discussions. We acknowledge financial support from the National Natural Science Foundation of China grant 11673010 (H.L., B.L.), National Key R&D Program of China grant 2016YFA0400702 (H.L., B.L.), National Thousand Young Talents program of China (B.L.). W.N.B acknowledges support from *Chandra* X-ray Center grant GO5-16089X, the NASA ADP Program, and the Penn State ACIS Instrument Team Contract SV4-74018 (issued by the *Chandra* X-ray Center, which is operated by the Smithsonian Astrophysical Observatory for and on behalf of NASA under contract NAS8-03060). S.C.G thanks the Discovery Grant Program of the Natural Science and Engineering Research Council of Canada.

The Guaranteed Time Observations (GTO) for the quasars studied were selected by the ACIS Instrument Principal Investigator, Gordon P. Garmire, currently of the Huntingdon Institute for X-ray Astronomy, LLC, which is under contract to the Smithsonian Astrophysical Observatory; Contract SV2-82024.

## REFERENCES

- Allen, J. T., Hewett, P. C., Maddox, N., Richards, G. T., & Belokurov, V. 2011, *MNRAS*, 410, 860
- Arnaud, K. A. 1996, in *Astronomical Society of the Pacific Conference Series*, Vol. 101, *Astronomical Data Analysis Software and Systems V*, ed. G. H. Jacoby & J. Barnes, 17
- Baskin, A., Laor, A., & Stern, J. 2014, *MNRAS*, 445, 3025
- Bianchi, S., Marinucci, A., Matt, G., et al. 2017, *MNRAS*, 468, 2740
- Brandt, W. N., & Alexander, D. M. 2015, *A&A Rev.*, 23, 1
- Broos, P. S., Feigelson, E. D., Townsley, L. K., et al. 2007, *ApJS*, 169, 353
- Cameron, E. 2011, *PASA*, 28, 128
- Cardelli, J. A., Clayton, G. C., & Mathis, J. S. 1989, *ApJ*, 345, 245
- Comastri, A. 2004, in *Astrophysics and Space Science Library*, Vol. 308, *Supermassive Black Holes in the Distant Universe*, ed. A. J. Barger, 245
- Comastri, A., Ranalli, P., Iwasawa, K., et al. 2011, *A&A*, 526, L9
- Dickey, J. M., & Lockman, F. J. 1990, *ARA&A*, 28, 215
- Dietrich, M., Mathur, S., Grupe, D., & Komossa, S. 2009, *ApJ*, 696, 1998
- Done, C. 2010, *ArXiv e-prints*, arXiv:1008.2287
- Fabian, A. C., Alston, W. N., Cackett, E. M., et al. 2017, *Astronomische Nachrichten*, 338, 269

- Fan, L. L., Wang, H. Y., Wang, T., et al. 2009, *ApJ*, 690, 1006
- Freeman, P. E., Kashyap, V., Rosner, R., & Lamb, D. Q. 2002, *ApJS*, 138, 185
- Gallagher, S. C., Brandt, W. N., Chartas, G., & Garmire, G. P. 2002, *ApJ*, 567, 37
- Gallagher, S. C., Brandt, W. N., Chartas, G., et al. 2006, *ApJ*, 644, 709
- Gallagher, S. C., Hines, D. C., Blaylock, M., et al. 2007, *ApJ*, 665, 157
- Gandhi, P., Lansbury, G. B., Alexander, D. M., et al. 2014, *ApJ*, 792, 117
- Garmire, G. P., Bautz, M. W., Ford, P. G., Nousek, J. A., & Ricker, Jr., G. R. 2003, in *Proc. SPIE*, Vol. 4851, *X-Ray and Gamma-Ray Telescopes and Instruments for Astronomy.*, ed. J. E. Truemper & H. D. Tananbaum, 28–44
- Gehrels, N. 1986, *ApJ*, 303, 336
- George, I. M., & Fabian, A. C. 1991, *MNRAS*, 249, 352
- Gibson, R. R., Brandt, W. N., & Schneider, D. P. 2008, *ApJ*, 685, 773
- Gibson, R. R., Jiang, L., Brandt, W. N., et al. 2009, *ApJ*, 692, 758
- Gilfanov, M., & Merloni, A. 2014, *Space Sci. Rev.*, 183, 121
- Hao, H., Elvis, M., Civano, F., & Lawrence, A. 2011, *ApJ*, 733, 108
- Hewett, P. C., & Foltz, C. B. 2003, *AJ*, 125, 1784
- Hewett, P. C., Foltz, C. B., & Chaffee, F. H. 1995, *AJ*, 109, 1498
- Ivezić, Ž., Menou, K., Knapp, G. R., et al. 2002, *AJ*, 124, 2364
- Jiang, L., Fan, X., Brandt, W. N., et al. 2010, *Nature*, 464, 380
- Just, D. W., Brandt, W. N., Shemmer, O., et al. 2007, *ApJ*, 665, 1004
- Kraft, R. P., Burrows, D. N., & Nousek, J. A. 1991, *ApJ*, 374, 344
- Leighly, K. M., Halpern, J. P., Jenkins, E. B., & Casebeer, D. 2007a, *ApJS*, 173, 1
- Leighly, K. M., Halpern, J. P., Jenkins, E. B., et al. 2007b, *ApJ*, 663, 103
- Luo, B., Brandt, W. N., Alexander, D. M., et al. 2013, *ApJ*, 772, 153
- . 2014, *ApJ*, 794, 70
- Luo, B., Brandt, W. N., Hall, P. B., et al. 2015, *ApJ*, 805, 122
- Luo, B., Brandt, W. N., Xue, Y. Q., et al. 2017, *ApJS*, 228, 2
- Lusso, E., Comastri, A., Vignali, C., et al. 2010, *A&A*, 512, A34
- Lyons, L. 1991, *A Practical Guide to Data Analysis for Physical Science Students*, 107
- Lyu, J., Rieke, G. H., & Shi, Y. 2017, *ApJ*, 835, 257
- Martin, D. C., Fanson, J., Schiminovich, D., et al. 2005, *ApJ*, 619, L1
- Mateos, S., Carrera, F. J., Page, M. J., et al. 2010, *A&A*, 510, A35
- Matt, G., Bianchi, S., Guainazzi, M., Barcons, X., & Panessa, F. 2012, *A&A*, 540, A111
- Mathews, J. H., Knigge, C., Long, K. S., et al. 2016, *MNRAS*, 458, 293
- Miller, B. P., Brandt, W. N., Schneider, D. P., et al. 2011, *ApJ*, 726, 20
- Murphy, K. D., & Yaqoob, T. 2009, *MNRAS*, 397, 1549
- Murray, N., Chiang, J., Grossman, S. A., & Voit, G. M. 1995, *ApJ*, 451, 498
- O'Donnell, J. E. 1994, *ApJ*, 422, 158
- Park, T., Kashyap, V. L., Siemiginowska, A., et al. 2006, *ApJ*, 652, 610
- Planck Collaboration, Ade, P. A. R., Aghanim, N., et al. 2016, *A&A*, 594, A13
- Plotkin, R. M., Gallo, E., Haardt, F., et al. 2016, *ApJ*, 825, 139
- Proga, D. 2005, *ApJ*, 630, L9
- Proga, D., Stone, J. M., & Kallman, T. R. 2000, *ApJ*, 543, 686
- Reeves, J. N., Turner, M. J. L., Ohashi, T., & Kii, T. 1997, *MNRAS*, 292, 468
- Reichard, T. A., Richards, G. T., Schneider, D. P., et al. 2003, *AJ*, 125, 1711
- Richards, G. T., Lacy, M., Storrie-Lombardi, L. J., et al. 2006, *ApJS*, 166, 470
- Rieke, G. H., Young, E. T., Engelbracht, C. W., et al. 2004, *ApJS*, 154, 25
- Rovilos, E., Georgantopoulos, I., Akylas, A., et al. 2014, *MNRAS*, 438, 494
- Schneider, D. P., Richards, G. T., Hall, P. B., et al. 2010, *AJ*, 139, 2360
- Scott, A. E., Stewart, G. C., Mateos, S., et al. 2011, *MNRAS*, 417, 992
- Shen, Y., Richards, G. T., Strauss, M. A., et al. 2011, *ApJS*, 194, 45
- Simmonds, C., Bauer, F. E., Thuan, T. X., et al. 2016, *A&A*, 596, A64
- Skrutskie, M. F., Cutri, R. M., Stiening, R., et al. 2006, *AJ*, 131, 1163
- Sprayberry, D., & Foltz, C. B. 1992, *ApJ*, 390, 39
- Steffen, A. T., Strateva, I., Brandt, W. N., et al. 2006, *AJ*, 131, 2826
- Stoeck, J. T., Morris, S. L., Weymann, R. J., & Foltz, C. B. 1992, *ApJ*, 396, 487
- Teng, S. H., Brandt, W. N., Harrison, F. A., et al. 2014, *ApJ*, 785, 19
- Trump, J. R., Hall, P. B., Reichard, T. A., et al. 2006, *ApJS*, 165, 1
- Vanden Berk, D. E., Richards, G. T., Bauer, A., et al. 2001, *AJ*, 122, 549
- Weymann, R. J., Morris, S. L., Foltz, C. B., & Hewett, P. C. 1991, *ApJ*, 373, 23
- Wright, E. L., Eisenhardt, P. R. M., Mainzer, A. K., et al. 2010, *AJ*, 140, 1868
- Xue, Y. Q., Luo, B., Brandt, W. N., et al. 2011, *ApJS*, 195, 10
- York, D. G., Adelman, J., Anderson, Jr., J. E., et al. 2000, *AJ*, 120, 1579
- Young, M., Elvis, M., & Risaliti, G. 2009, *ApJS*, 183, 17
- Yuan, M. J., & Wills, B. J. 2003, *ApJ*, 593, L11

**Table 2**  
X-ray Photometric Properties

Object Name	Net Counts		Band	$\Gamma_{\text{eff}}$	$\Gamma_{\text{XSPEC}}$	Flux ( $10^{-14} \text{ erg cm}^{-2} \text{ s}^{-1}$ )		$\log L_X$ ( $\text{erg s}^{-1}$ )
(LBQS B) (1)	0.5–2 keV (2)	2–8 keV (3)	Ratio (4)	(5)	(6)	0.5–2 keV (7)	2–8 keV (8)	2–10 keV (9)
0021–0213	$6.4^{+4.6}_{-2.6}$	$5.9^{+4.9}_{-2.7}$	$0.91^{+1.57}_{-0.44}$	$1.0^{+0.5}_{-0.7}$	$1.2^{+0.4}_{-0.6}$	0.12	0.46	43.9
1203+1530	$7.2^{+3.9}_{-2.7}$	$1.9^{+2.9}_{-1.4}$	$0.26^{+0.68}_{-0.11}$	$2.2^{+0.9}_{-0.9}$	$2.0^{+0.6}_{-0.7}$	0.21	0.17	43.6
1212+1445	$4.1^{+3.3}_{-2.0}$	$5.2^{+3.7}_{-2.4}$	$1.28^{+2.35}_{-0.58}$	$0.7^{+0.6}_{-0.8}$	$0.5^{+0.6}_{-0.6}$	0.13	0.81	43.8
1235+1453	$4.0^{+3.3}_{-2.0}$	$6.6^{+4.0}_{-2.7}$	$1.63^{+2.73}_{-0.71}$	$0.4^{+0.5}_{-0.8}$	$0.8^{+0.6}_{-0.6}$	0.11	0.96	44.1
1442–0011	$5.1^{+3.3}_{-2.2}$	$2.0^{+2.9}_{-1.4}$	$0.39^{+1.00}_{-0.16}$	$1.9^{+0.9}_{-0.8}$	$1.8^{+0.9}_{-0.7}$	0.19	0.24	44.0
1443+0141	$24.9^{+6.2}_{-5.1}$	$10.7^{+4.7}_{-3.4}$	$0.43^{+0.65}_{-0.30}$	$1.7^{+0.4}_{-0.3}$	$1.2^{+0.3}_{-0.3}$	0.79	1.25	44.7
2201–1834	< 4.0	< 4.1	...	...	...	< 0.13	< 0.70	< 43.8

**Note.** — Col. (1): object name. Cols. (2)–(3): net counts in the observed soft (0.5–2 keV) and hard (2–8 keV) bands. Col. (4): ratio between the soft-band and hard-band counts, the symbol "..." indicates that the source is undetected in both the soft and hard bands. Col. (5): effective power-law photon index derived from the photometric approach. These values were used in our analyses and discussions. Col. (6): best-fit power-law photon index obtained from spectral fitting. Cols. (7)–(8): Galactic absorption-corrected flux in the soft (0.5–2 keV) and hard (2–8 keV) bands. Col. (9): logarithm of the rest-frame 2–10 keV luminosity, derived from the 0.5–2 keV flux.

**Table 3**  
X-ray and Optical Properties

Object Name (LBQS B) (1)	Count Rate (0.5–2 keV) (2)	$f_{2\text{keV,soft}}$ (3)	$f_{2\text{keV,hard}}$ (4)	$f_{2500 \text{ \AA}}$ (5)	$\log L_{2500 \text{ \AA}}$ (6)	$\alpha_{\text{OX,soft}}$ (7)	$\alpha_{\text{OX,hard}}$ (8)	$\Delta\alpha_{\text{OX,soft}}(\sigma)$ (9)	$\Delta\alpha_{\text{OX,hard}}(\sigma)$ (10)	$f_{\text{weak}}$ (11)
0021–0213	$0.18^{+0.13}_{-0.07}$	0.32	1.81	2.34	31.46	$-2.25^{+0.12}_{-0.07}$	$-1.96^{+0.14}_{-0.08}$	–0.58(3.95)	–0.29(1.99)	$5.7^{+3.3}_{-3.2}$
1203+1530	$0.38^{+0.21}_{-0.14}$	0.90	0.71	1.68	31.05	$-2.02^{+0.09}_{-0.06}$	$-2.06^{+0.25}_{-0.12}$	–0.41(2.79)	–0.45(3.07)	$14.7^{+16.4}_{-11.5}$
1212+1445	$0.26^{+0.21}_{-0.13}$	0.31	2.28	4.46	31.47	$-2.36^{+0.13}_{-0.08}$	$-2.03^{+0.12}_{-0.08}$	–0.69(4.73)	–0.36(2.44)	$8.5^{+4.9}_{-4.4}$
1235+1453	$0.22^{+0.18}_{-0.11}$	0.19	3.54	1.48	31.38	$-2.26^{+0.14}_{-0.08}$	$-1.77^{+0.10}_{-0.07}$	–0.60(4.13)	–0.11(0.77)	$2.0^{+1.0}_{-0.9}$
1442–0011	$0.34^{+0.24}_{-0.15}$	0.86	1.13	3.45	31.60	$-2.15^{+0.11}_{-0.07}$	$-2.11^{+0.24}_{-0.12}$	–0.46(3.15)	–0.41(2.83)	$11.9^{+12.6}_{-9.2}$
1443+0141	$1.55^{+0.39}_{-0.32}$	3.50	6.12	2.28	31.50	$-1.85^{+0.04}_{-0.03}$	$-1.75^{+0.07}_{-0.05}$	–0.17(1.16)	–0.08(0.53)	$1.6^{+0.6}_{-0.6}$
2201–1834	< 0.29	< 0.37	< 2.29	9.40	31.88	< –2.46	< –2.15	< –0.73(4.99)	< –0.42(2.91)	> 12.8

**Note.** — Col. (1): object name. Col. (2): 0.5–2 keV count rate in units of  $10^{-3} \text{ s}^{-1}$ . Col. (3): soft-band derived flux density at rest-frame 2 keV in units of  $10^{-32} \text{ erg cm}^{-2} \text{ s}^{-1} \text{ Hz}^{-1}$ , derived using the measured  $\Gamma_{\text{eff}}$  and the soft-band flux. Col. (4): hard-band derived flux density at rest-frame 2 keV in units of  $10^{-32} \text{ erg cm}^{-2} \text{ s}^{-1} \text{ Hz}^{-1}$ , derived using  $\Gamma = 2$  and the hard-band flux. Col. (5): flux density at rest-frame 2500 Å in units of  $10^{-27} \text{ erg cm}^{-2} \text{ s}^{-1} \text{ Hz}^{-1}$ , adopted from Gallagher et al. (2006). Col. (6): logarithm of the rest-frame 2500 Å monochromatic luminosity in units of  $\text{erg s}^{-1} \text{ Hz}^{-1}$ , adopted from Gallagher et al. (2006). Col. (7): soft-band derived  $\alpha_{\text{OX}}$  parameter, derived using  $f_{2\text{keV,soft}}$ . Col. (8): hard-band derived  $\alpha_{\text{OX}}$  parameter, derived using  $f_{2\text{keV,hard}}$ . Col. (9): difference between the soft-band derived  $\alpha_{\text{OX}}$  and the expected  $\alpha_{\text{OX}}$  from the Steffen et al. (2006)  $\alpha_{\text{OX}}-L_{2500 \text{ \AA}}$  relation. The statistical significance of this difference, measured in units of the  $\alpha_{\text{OX}}$  rms scatter in Table 5 of Steffen et al. (2006), is given in the parenthesis. Col. (10): difference between the hard band derived  $\alpha_{\text{OX}}$  and the expected  $\alpha_{\text{OX}}$ . Col. (11): factor of hard-band X-ray weakness in accordance with  $\Delta\alpha_{\text{OX,hard}}$ . The errors were derived from the errors of  $\alpha_{\text{OX,hard}}$ .